

# South Greenland ice-sheet collapse during Marine Isotope Stage 11

Alberto V. Reyes<sup>1,2†</sup>, Anders E. Carlson<sup>1,3</sup>, Brian L. Beard<sup>1</sup>, Robert G. Hatfield<sup>3</sup>, Joseph S. Stoner<sup>3</sup>, Kelsey Winsor<sup>1</sup>, Bethany Welke<sup>1†</sup> & David J. Ullman<sup>1,3</sup>

Varying levels of boreal summer insolation and associated Earth system feedbacks led to differing climate and ice-sheet states during late-Quaternary interglaciations. In particular, Marine Isotope Stage (MIS) 11 was an exceptionally long interglaciation and potentially had a global mean sea level 6 to 13 metres above the present level around 410,000 to 400,000 years ago<sup>1,2</sup>, implying substantial mass loss from the Greenland ice sheet (GIS). There are, however, no model simulations and only limited proxy data<sup>3,4</sup> to constrain the magnitude of the GIS response to climate change during this ‘super interglacial’<sup>5</sup>, thus confounding efforts to assess climate/ice-sheet threshold behaviour<sup>6,7</sup> and associated sea-level rise<sup>1,2</sup>. Here we show that the south GIS was drastically smaller during MIS 11 than it is now, with only a small residual ice dome over southernmost Greenland. We use the strontium–neodymium–lead isotopic composition of proglacial sediment discharged from south Greenland to constrain the provenance of terrigenous silt deposited on the Eirik Drift, a sedimentary deposit off the south Greenland margin. We identify a major reduction in sediment input derived from south Greenland’s Precambrian bedrock terranes, probably reflecting the cessation of subglacial erosion and sediment transport<sup>8</sup> as a result of near-complete deglaciation of south Greenland. Comparison with ice-sheet configurations from numerical models<sup>7,9–12</sup> suggests that the GIS lost about 4.5 to 6 metres of sea-level-equivalent volume during MIS 11. This is evidence for late-Quaternary GIS collapse after it crossed a climate/ice-sheet stability threshold that may have been no more than several degrees above pre-industrial temperatures<sup>6,7</sup>.

Little information is available on the magnitude of the retreat of the GIS or the Antarctic ice sheet (AIS) during MIS 11, thus hindering efforts to understand potentially nonlinear responses of Earth’s ice sheets to protracted warm intervals. AIS retreat could explain all of the proposed +6–13 m MIS 11 sea-level range<sup>1,13</sup>. Alternatively, near-complete GIS deglaciation would account for the lower-end estimate of the sea-level highstand<sup>14</sup>, with some AIS contribution required for a highstand greater than +7 m. Yet another possibility is that the GIS and AIS experienced minimal retreat during MIS 11, consistent with reconstructions suggesting that MIS 11 sea level may not have been appreciably different from today<sup>2</sup>. Thus, constraints on the MIS 11 response of the GIS can shed considerable light on uncertain palaeo-sea-level records, sparse palaeoclimate proxy data<sup>5</sup> and the possibility that the modelled temperature threshold for GIS collapse<sup>6,7</sup> may have been exceeded during MIS 11. In the absence of direct geomorphic evidence for the magnitude of ice-sheet retreat during past interglaciations, we turn to geochemical proxy evidence to assess the south GIS response to MIS 11 climate change and, in turn, estimate the GIS contribution to MIS 11 sea level.

We use the sedimentary record of Eirik Drift core MD99-2227 (Figs 1 and 2) to infer GIS extent on south Greenland, where many models suggest interglacial ice-sheet mass loss will be most pronounced<sup>9–12</sup>. The Eirik Drift receives terrigenous sediment from subglacial erosion of south

Greenland’s Precambrian bedrock (the Ketilidian Mobile Belt (KMB), Archaean Block (AB) and Nagsstugtoqidian Mobile Belt (NMB)) and Palaeogene volcanics that outcrop in east Greenland and Iceland (Fig. 1). These sediments are transported to the core site in the Western Boundary Undercurrent<sup>15–17</sup> (Fig. 1 and Methods), and magnetic and geochemical properties of Holocene Eirik Drift sediments document the close coupling between GIS subglacial erosion, sediment transport and terrigenous silt deposition at MD99-2227<sup>16–18</sup>. Other potential sources of terrigenous silt at Eirik Drift, including northeast Greenland, Scotland, Scandinavia and re-transported silt in Arctic sea ice, are likely to be negligible (Methods).

We estimate the provenance of the carbonate-free detrital silt fraction in Eirik Drift sediments using Sr–Nd–Pb isotope ratios, which trace terrestrial silt sources because the unique isotope compositions of south Greenland’s bedrock terranes reflect their differing ages and

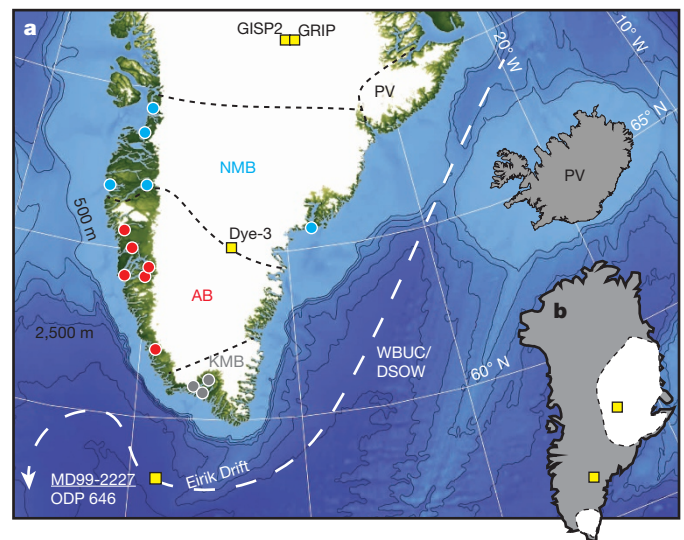


**Figure 1 | Map of Greenland and other features mentioned in the text.** **a**, Bedrock terrane boundaries (black dashed lines) and sampling sites for Greenland stream sediments (filled circles; multiple sites per symbol); KMB, Ketilidian Mobile Belt (grey); AB, Archaean Block (red); NMB, Nagsstugtoqidian Mobile Belt (blue); PV, Palaeogene volcanics. Yellow squares mark locations of marine sediment core MD99-2227 and Dye-3 and Summit (GISP2, GRIP) ice cores. Dashed white lines denote modern deep-water circulation features that are thought to have been active during past interglaciations<sup>15–21</sup>; DSOW, Denmark Strait Overflow Water; WBUC, Western Boundary Undercurrent. The bathymetric contour interval is 500 m. **b**, Inset map. White polygons show the potential configuration of the MIS 11 Greenland ice sheet, which is similar to modelled ice limits representing ~6 m of sea-level-equivalent mass loss<sup>7</sup> (Methods). Yellow squares are ice-core sites shown in **a**.

<sup>1</sup>Department of Geoscience, University of Wisconsin-Madison, 1215 West Dayton Street, Madison, Wisconsin 53706, USA. <sup>2</sup>School of Geography, Archaeology and Palaeoecology, Queen’s University Belfast, Elmwood Avenue, Belfast BT7 1NN, UK. <sup>3</sup>College of Earth, Ocean, and Atmospheric Sciences, Oregon State University, 104 CEOAS Administration Building, Corvallis, Oregon 97331, USA. †Present addresses: Department of Earth and Atmospheric Sciences, University of Alberta, Edmonton, Alberta T6G 2E3, Canada (A.V.R.); Department of Geosciences, University of Arizona, 1040 East 4th Street, Tucson, Arizona 85721, USA (B.W.).

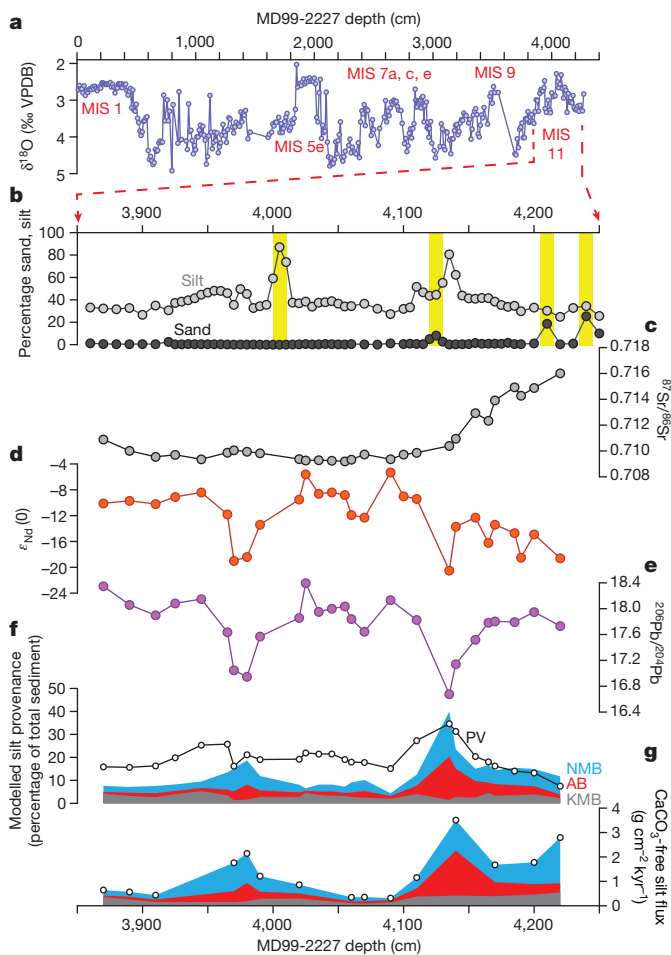


**Figure 2** | MD99-2227 records on depth scale. **a**, Full  $\delta^{18}\text{O}$  *Neogloboquadrina pachyderma* (sinistral) record<sup>19</sup>; interglacial MISs are indicated.  $\delta^{18}\text{O} = 1,000 \times [({}^{18}\text{O}/{}^{16}\text{O})_{\text{sample}}/({}^{18}\text{O}/{}^{16}\text{O})_{\text{VPDB}} - 1]$ ; VPDB, Vienna PeeDee belemnite. **b**, Weight per cent silt and sand. Vertical yellow bars denote ice-rafted debris and turbidite layers<sup>19</sup> that are not included in silt provenance estimates. **c–e**, Isotopic composition, with analytical uncertainty smaller than symbol size:  ${}^{87}\text{Sr}/{}^{86}\text{Sr}$  (**c**);  $\epsilon_{\text{Nd}}$  (**d**; Methods);  ${}^{207}\text{Pb}/{}^{204}\text{Pb}$  (**e**).  ${}^{207}\text{Pb}/{}^{204}\text{Pb}$  and  ${}^{208}\text{Pb}/{}^{204}\text{Pb}$  follow a similar trend (Supplementary Table 1) and are not shown here. **f**, Median inferred silt provenance from isotope mixing model, expressed as percentage of total sediment. Provenance estimates do not sum to 100% because they do not include clay or sand size fractions. **g**, Estimated flux of  $\text{CaCO}_3$ -free silt from south Greenland Precambrian terranes (upper and lower uncertainty estimates in Extended Data Fig. 2).

tectonometamorphic histories<sup>16</sup> (Methods and Extended Data Fig. 1). Silt from KMB sources is readily distinguished from the AB and NMB by higher  ${}^{206}\text{Pb}/{}^{204}\text{Pb}$ ,  ${}^{207}\text{Pb}/{}^{204}\text{Pb}$  and  $\epsilon_{\text{Nd}}$  values (Methods). The AB and NMB are more similar isotopically, although AB silts tend towards higher  ${}^{87}\text{Sr}/{}^{86}\text{Sr}$ , and lower  ${}^{207}\text{Pb}/{}^{204}\text{Pb}$  and  ${}^{208}\text{Pb}/{}^{204}\text{Pb}$ , than do NMB silts. Silts derived from Palaeogene volcanic rocks have very low  ${}^{87}\text{Sr}/{}^{86}\text{Sr}$  and high  $\epsilon_{\text{Nd}}$ , compared with the three Precambrian terranes.

The MD99-2227  $\delta^{18}\text{O}$  stratigraphy indicates the presence of MIS 11 sediments below  $\sim 3,950$  cm core depth, and an age–depth model based on  $\delta^{18}\text{O}$  and relative geomagnetic palaeointensity suggests that the base of MD99-2227 dates to late MIS 12<sup>19</sup> (Fig. 2a and Methods). The  ${}^{87}\text{Sr}/{}^{86}\text{Sr}$  ratio decreases from  $\sim 0.717$  to  $\sim 0.709$  between depths of 4,240 and 4,090 cm (Fig. 2c). The  ${}^{87}\text{Sr}/{}^{86}\text{Sr}$  ratio stays at or below  $\sim 0.709$  until 3,990 cm, where it increases to  $\sim 0.711$  near the end of MIS 11. Though the  $\epsilon_{\text{Nd}}$  data are more variable (Fig. 2d), with two excursions to low  $\epsilon_{\text{Nd}}$  at 4,135 and  $\sim 3,975$  cm,  $\epsilon_{\text{Nd}}$  follows a general increasing trend from  $-20.9$  to  $-5.3$  between 4,240 and 4,090 cm, followed by a return to lower  $\epsilon_{\text{Nd}}$  at the end of MIS 11. The Pb isotope data mimic the  $\epsilon_{\text{Nd}}$  trend through MIS 11 (Fig. 2e).

Because south Greenland Precambrian terranes have distinctly high  ${}^{87}\text{Sr}/{}^{86}\text{Sr}$  and low  $\epsilon_{\text{Nd}}$ , the Sr and Nd isotope data are consistent with an overall reduction in silt derived from south Greenland's Precambrian bedrock. Direct interpretation of the Pb data is complicated by anomalous KMB Pb isotope compositions relative to the AB and NMB (Extended Data Fig. 1). We use an isotope mixing model to estimate the proportion and flux of silt derived from each south Greenland terrane, based on the median solution from 10,000 model runs (Fig. 2f, g and Methods). The Palaeogene volcanic silt fraction of the total sediment increases from  $\sim 10\%$  during late MIS 12 to 15–30% during MIS 11 (Fig. 2f), which probably reflects intensification of the Western Boundary Undercurrent during interglaciations<sup>15–21</sup>. Precambrian silt is initially 10–15% of the total sediment during MIS 12, with an increase to  $\sim 40\%$  at 4,135 cm early in MIS 11 that is mainly driven by increases in the AB and NMB fractions. Precambrian silt decreases to 4–8% of the total sediment for the middle of MIS 11 (4,090–4,020 cm), and then increases again, to  $\sim 20\%$  at 3,980 cm, with a subsequent return to  $\sim 5\%$  at the end of MIS 11. Because inferred KMB contributions remain relatively constant during this interval, at  $<4\%$  of total sediment, the decrease in Precambrian silt sedimentation above 4,110 cm is driven mainly by changes in silt sourced from the AB and NMB terranes.

Sediment flux estimates (Fig. 2g, Methods and Extended Data Fig. 2) corroborate the provenance interpretations based on the percentage of total sediment. Silt flux from south Greenland's Precambrian bedrock is  $1.7\text{--}3.5\text{ g cm}^{-2}\text{ kyr}^{-1}$  during late MIS 12 and into MIS 11, but decreases by an order of magnitude to  $\sim 0.3\text{ g cm}^{-2}\text{ kyr}^{-1}$  during MIS 11. Flux from the KMB during MIS 11 is low, but does not decrease as precipitously as flux from the AB or NMB, both of which decrease to a flux of less than  $\sim 0.1\text{ g cm}^{-2}\text{ kyr}^{-1}$ .

Comparing our terrane provenance record with similar estimates for the last interglaciation (LIG; 128–116 kyr ago) and the Holocene epoch<sup>16</sup>, we find that the Precambrian silt contribution at the end of MIS 12 is similar to sedimentation during the penultimate and last deglaciations (Fig. 3b, c). Precambrian silt early in MIS 11 is largely derived from the NMB and AB, and probably reflects increased ablation and attendant discharge of silt from the south GIS, similar to early LIG and Holocene silt pulses<sup>16</sup>. The low in Precambrian silt during the MIS 11  $\delta^{18}\text{O}$  minimum (Fig. 3a) is unprecedented with respect to these later interglaciations (Fig. 3b). The near-complete loss of NMB- and AB-derived silt drives this minimum, with individual terrane contributions decreasing to  $<1\%$  of total sediment. For comparison, the minimum NMB + AB fraction is 10–15% of the total sediment during the Holocene and LIG (Fig. 3b). Although it is not appropriate to compare sediment flux during the Holocene and Termination I owing to stretching in the upper part of MD99-2227<sup>19</sup> (Methods), terrigenous silt flux from south Greenland's Precambrian bedrock was over an order of magnitude higher in the LIG than during MIS 11 (Fig. 3c).

One explanation for the near absence of NMB and AB silt during the MIS 11  $\delta^{18}\text{O}$  minimum is that a change in ocean circulation reduced or stopped transport of NMB and AB sediment to Eirik Drift. However, the continued input of KMB and Palaeogene volcanic silt suggests that sediment transport pathways to Eirik Drift during MIS 11 were similar to other interglaciations<sup>15,16,21</sup>. Alternatively, ablation, meltwater production and subglacial erosion are high during ice-sheet retreat<sup>8</sup>, but complete ice loss from a given terrane would lead to the cessation of subglacial erosion and meltwater transport of silt and, in turn, to decreased sediment flux to the ocean. We therefore interpret the near absence of NMB and AB silt during the MIS 11  $\delta^{18}\text{O}$  minimum as indicating the loss of ice from these terranes. Deglaciated terranes may supply minor amounts of silt even during periods of minimal or absent GIS coverage, owing to paraglacial processes that entrain and transport glacial sediment in recently deglaciated areas<sup>22,23</sup>. The relatively consistent MIS 11 KMB silt flux may suggest persistent valley glaciers or local ice caps, or both, on that terrane, perhaps due to regionally high snow accumulation<sup>24</sup>. The NMB and AB silt increase at the end of MIS 11 implies south GIS regrowth, and an associated increase in subglacial erosion<sup>8</sup> and

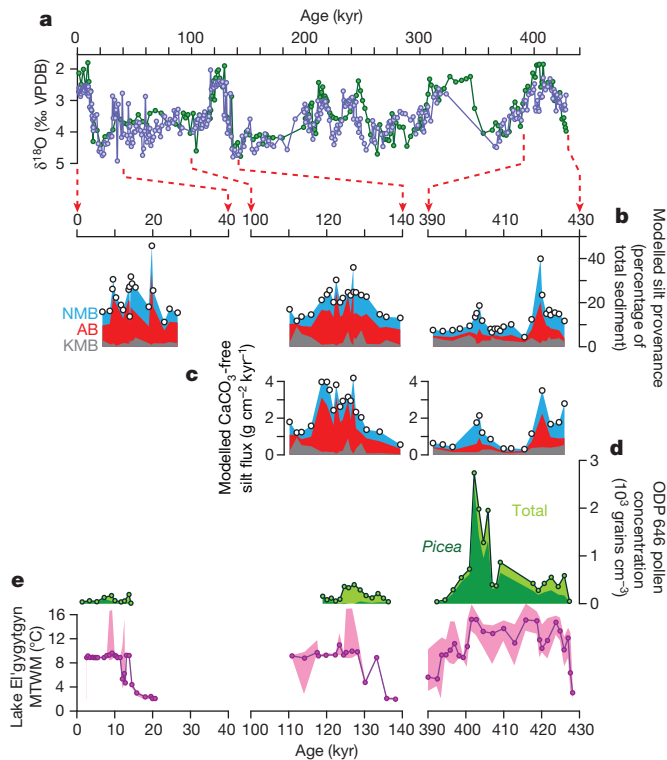


**Figure 3 | Terrigenous silt provenance estimates for MD99-2227 compared with other Eirik Drift indicators of GIS extent during the Holocene, LIG and MIS 11.** Age model uncertainties preclude direct assessment of millennial-scale leads and lags for the LIG and MIS 11. **a**, *Neoglobobquadrina pachyderma* (*s*)  $\delta^{18}\text{O}$  from ODP Site 646 (ref. 4; green) and MD99-2227 (Methods; blue). **b**, **c**, MD99-2227 median inferred silt provenance estimated from isotope mixing model, expressed as percentage of total sediment (**b**) and flux of  $\text{CaCO}_3$ -free silt (**c**). Holocene and LIG values are recast from Sr–Nd–Pb isotope composition in ref. 16. Holocene flux data are not presented owing to stretching in the upper 15 m of MD99-2227<sup>19</sup>. **d**, ODP Site 646 pollen data<sup>3</sup>, showing *Picea* (dark green) and total (minus *Pinus*; light green) pollen concentrations. For general comparison only, we plot ODP Site 646 data on the MD99-2227 age model, using magnetic susceptibility to correlate the two cores (Extended Data Fig. 4; Methods). **e**, Reconstructed mean temperature of the warmest month (MTWM) at Lake El'gygytyn, Russia<sup>5</sup>. Upper and lower bounds of shaded interval denote maximum and minimum warmest-month reconstructed temperatures, respectively.

glaciofluvial sediment transport<sup>18,22,23</sup> on those terranes. Ablation would subsequently decrease as climate further cooled into the next glacial stage, leading to reduced subglacial erosion and meltwater discharge. This pattern is consistent with lower Greenland Precambrian silt sedimentation at the end of MIS 11, and is similar to trends at the end of the LIG<sup>16</sup> (Fig. 3b, c).

An Eirik Drift pollen record from Ocean Drilling Program (ODP) Site 646 (Fig. 1) shows the highest pollen concentrations of the past  $\sim 1,000$  kyr and abundant *Picea* (spruce) pollen during the  $\delta^{18}\text{O}$  minimum of MIS 11<sup>4</sup> (Fig. 3d), but these data do not relate directly to GIS extent and volume. Sedimentary ancient DNA recovered from silty ice at the base of the Dye-3 ice core (Fig. 1) is evidence for ice-free, forested conditions at one location on south Greenland<sup>3</sup>, but age estimates for the DNA-bearing silty ice span  $\sim 400$  kyr to  $>1,000$  kyr and thus preclude direct assignment to MIS 11. We now show that south Greenland was nearly completely deglaciated during MIS 11, providing the ice-free conditions required for development of boreal forest<sup>3,4</sup>. In contrast, basal ice from Summit Station (Fig. 1) probably pre-dates  $\sim 400$  kyr ago<sup>3,25</sup>, indicating survival of the central GIS during MIS 11. Similarly, continuous MIS 11 deposition of ice-rafted debris in the western Iceland Sea, following the Termination V peak in ice-rafted debris across the polar

North Atlantic, suggests the presence of marine-terminating ice on east-central and northeast Greenland during MIS 11<sup>26,27</sup>.

We compare these constraints on MIS 11 GIS extent (see, for example, Fig. 1b) with ice-sheet models that simulate GIS response to past and future climate warming, to qualitatively assess potential GIS contribution to MIS 11 sea level. Models with ice absence on the NMB and AB terranes simulate a GIS contribution to sea-level rise of  $>4.5$  m (refs 9–12), whereas the maximum modelled GIS retreat consistent with our interpretation of an ice-free AB and NMB and other geological constraints<sup>3,25–27</sup> yields  $\sim 6$  m of GIS sea-level contribution<sup>7</sup>. South GIS retreat could therefore account for all, or most, of the minimum estimated MIS 11 sea-level highstand of  $\sim 6$  m (ref. 1) and is within the  $1\sigma$  uncertainty envelope of the Red Sea sea-level record<sup>2</sup>, implying a relatively stable AIS. Alternatively, the upper end of MIS 11 sea-level estimates implies complete collapse of the West AIS and at least some mass loss from the East AIS<sup>12</sup>, in addition to 4.5–6 m of GIS sea-level contribution.

Evidence for deglaciation of south Greenland consequently suggests that a climate/ice-stability threshold was crossed during MIS 11. Coupled climate/ice-sheet models simulate a threshold for complete GIS melting of 1.7–2.0 °C of warming relative to the preindustrial late Holocene if positive dynamic feedbacks are considered<sup>6,7</sup>. They also simulate a long GIS response time for temperature increases approaching the 1.7–2.0 °C threshold. However, the GIS response is considerably more rapid under  $\sim 4$  °C warming scenarios, with complete collapse in  $\sim 8$  kyr. Unfortunately, available proxy records offer conflicting evidence for the Arctic palaeoclimate during MIS 11. The few existing temperature reconstructions from near central-south Greenland suggest that MIS 11 climate was no warmer than peak early Holocene or LIG climate<sup>4,26</sup>. In contrast, Siberian pollen records<sup>5</sup> suggest 4–5 °C of summer warming relative to the early Holocene and LIG (Fig. 3e). Limited field evidence indicates that continuous permafrost may have thawed during MIS 11 at a site in Siberia<sup>28</sup>, although permafrost persisted locally through this interval in northern Canada<sup>29</sup>. In the Arctic Ocean, faunal records<sup>30</sup> imply that substantially warmer-than-present summer sea surface temperatures and seasonal—not perennial—sea-ice cover characterized MIS 11.

Our results therefore prompt us to ask why south Greenland deglaciated almost completely during MIS 11, when ice persisted through the LIG and the Holocene<sup>16</sup>. Anomalous MIS 11 Arctic warmth<sup>5</sup> and a seasonally ice-free ocean<sup>30</sup> could have pushed the GIS past an ice-stability threshold<sup>6,7</sup> that was not crossed during the LIG or early Holocene. Alternatively, protracted warmth during the long MIS 11 interglaciation may have allowed the GIS to respond fully to interglacial conditions that were similar to the early Holocene and LIG, with these later interglaciations being too short for comparable ice-sheet collapse. A more extensive network of Pleistocene climate and ice-extent records around Greenland is required to assess these alternative scenarios, which have important implications for predicting the long-term behaviour of the GIS in response to future climate change scenarios<sup>6,7</sup>. In this context, our evidence for a late-Quaternary collapse of the south GIS provides an important example of geologically recent ice-sheet instability and retreat under climate conditions within the range of those anticipated by the end of this century.

## METHODS SUMMARY

We supplemented an earlier compilation<sup>16</sup> of Greenland stream sediment isotope geochemistry with an additional 31 samples of fine-grained glaciofluvial sediment collected from southwest Greenland (Extended Data Fig. 3). Chemical separation and isotopic analyses were conducted at the University of Wisconsin–Madison Radiogenic Isotope Laboratory. Subsamples of the 3–63  $\mu\text{m}$  fraction of MIS 11 sediment from core MD99-2227 were twice leached with 0.1 M HCl to remove biogenic carbonate and authigenic Fe–Mn coatings. All samples were spiked with mixed Rb–Sr and rare-earth-element tracers, and then digested in Parr pressure vessels with hydrofluoric acid and  $\text{HNO}_3$ . Pb, Rb–Sr and rare-earth-element separation was by sequential ion-exchange column chromatography. Isotope ratios were measured on a VG Sector 54 thermal ionization mass spectrometer, with Rb, Sr, Nd and

Sm concentrations determined by isotope dilution. Procedural blanks were negligible compared with sample size.

The isotope mixing model has four terrane components (KMB, AB, NMB and Palaeogene volcanics) and five endmembers ( $^{87}\text{Sr}/^{86}\text{Sr}$ ,  $\epsilon_{\text{Nd}}$ ,  $^{206}\text{Pb}/^{204}\text{Pb}$ ,  $^{207}\text{Pb}/^{204}\text{Pb}$  and  $^{208}\text{Pb}/^{204}\text{Pb}$ ). The model was run 10,000 times, with endmember composition and concentration randomly selected within the 16.5–83.5% quantile range of the stream sediment data sets for each terrane. Mixing model results are corrected for  $\text{CaCO}_3$  content and presented as the median of all valid solutions returned by the 10,000 model runs, with 67% and 95% confidence intervals based on the 83.5–16.5% and 97.5–2.5% quantiles of all valid solutions, respectively (Extended Data Fig. 2).

**Online Content** Methods, along with any additional Extended Data display items and Source Data, are available in the online version of the paper; references unique to these sections appear only in the online paper.

Received 5 November 2013; accepted 2 May 2014.

- Raymo, M. E. & Mitrovica, J. X. Collapse of polar ice sheets during the stage 11 interglacial. *Nature* **483**, 453–456 (2012).
- Rohling, E. J. *et al.* Comparison between Holocene and Marine Isotope Stage-11 sea-level histories. *Earth Planet. Sci. Lett.* **291**, 97–105 (2010).
- Willerslev, E. *et al.* Ancient biomolecules from deep ice cores reveal a forested southern Greenland. *Science* **317**, 111–114 (2007).
- de Vernal, A. & Hillaire-Marcel, C. Natural variability of Greenland climate, vegetation, and ice volume during the past million years. *Science* **320**, 1622–1625 (2008).
- Melles, M. *et al.* 2.8 Million years of Arctic climate change from Lake El'gygytyn, NE Russia. *Science* **337**, 315–320 (2012).
- Ridley, J., Gregory, J. M., Huybrechts, P. & Lowe, J. Thresholds for irreversible decline of the Greenland ice sheet. *Clim. Dyn.* **35**, 1049–1057 (2010).
- Robinson, A., Calov, R. & Ganopolski, A. Multistability and critical thresholds of the Greenland ice sheet. *Nature Clim. Change* **2**, 429–432 (2012).
- Cowton, T., Nienow, P., Bartholomew, I., Sole, A. & Mair, D. Rapid erosion beneath the Greenland ice sheet. *Geology* **40**, 343–346 (2012).
- Cuffey, K. M. & Marshall, S. J. Substantial contribution to sea-level rise during the last interglacial from the Greenland Ice Sheet. *Nature* **404**, 591–594 (2000).
- Huybrechts, P. Sea-level changes at the LGM from ice-dynamic reconstructions of the Greenland and Antarctic ice sheets during the glacial cycles. *Quat. Sci. Rev.* **21**, 203–231 (2002).
- Tarasov, L. & Peltier, W. R. Greenland glacial history, borehole constraints, and Eemian extent. *J. Geophys. Res.* **108**, 2143 (2003).
- Lhomme, N., Clarke, G. K. C. & Marshall, S. J. Tracer transport in the Greenland Ice Sheet - constraints on ice cores and glacial history. *Quat. Sci. Rev.* **24**, 173–194 (2005).
- Fretwell, P. Bedmap2: improved ice bed, surface and thickness datasets for Antarctica. *Cryosphere* **7**, 375–393 (2013).
- Bamber, J. L. *et al.* A new bed elevation dataset for Greenland. *Cryosphere* **7**, 499–510 (2013).
- Fagel, N. & Hillaire-Marcel, C. Glacial/interglacial instabilities of the Western Boundary Under Current during the last 365 kyr from Sm/Nd ratios of the sedimentary clay-size fractions at ODP site 646 (Labrador Sea). *Mar. Geol.* **232**, 87–99 (2006).
- Colville, E. J. *et al.* Sr-Nd-Pb isotope evidence for ice-sheet presence on southern Greenland during the last interglacial. *Science* **333**, 620–623 (2011).
- Stoner, J. S., Channell, J. E. T. & Hillaire-Marcel, C. Magnetic properties of deep-sea sediments off southwest Greenland: evidence for major differences between the last two deglaciations. *Geology* **23**, 241–244 (1995).
- Carlson, A. E., Stoner, J. S., Donnelly, J. P. & Hillaire-Marcel, C. Response of the southern Greenland Ice Sheet during the last two deglaciations. *Geology* **36**, 359–362 (2008).
- Evans, H. F. *et al.* Paleointensity-assisted chronostratigraphy of detrital layers on the Eirik Drift (North Atlantic) since marine isotope stage 11. *Geochem. Geophys. Geosyst.* **8**, Q11007 (2007).
- Hillaire-Marcel, C., de Vernal, A. & McKay, J. Foraminifer isotope study of the Pleistocene Labrador Sea, northwest North Atlantic (IODP Sites 1302/03 and 1305), with emphasis on paleoceanographical differences between its “inner” and “outer” basins. *Mar. Geol.* **279**, 188–198 (2011).
- Hillaire-Marcel, C., de Vernal, A., Bilodeau, G. & Wu, G. Isotope stratigraphy, sedimentation rates, deep circulation, and carbonate events in the Labrador Sea during the last ~200 ka. *Can. J. Earth Sci.* **31**, 63–89 (1994).
- Hasholt, B. in *Proc. Int. Symp. Erosion Sediment Yield: Global Regional Perspectives* (eds Walling, D. E. & Webb, B. W.) 105–114 (IAHS-AISH Publication, 1996).
- Church, M. & Ryder, J. M. Paraglacial sedimentation: a consideration of fluvial processes conditioned by glaciation. *Geol. Soc. Am. Bull.* **83**, 3059–3071 (1972).
- Ohmura, A. & Reeh, N. New precipitation and accumulation maps for Greenland. *J. Glaciol.* **37**, 140–148 (1991).
- Bierman, P. R. *et al.* Preservation of a preglacial landscape under the center of the Greenland ice sheet. *Science* **344**, 402–405 (2014).
- Helmske, J. P. & Bauch, H. A. Comparison of conditions between the polar and subpolar North Atlantic region over the last five climate cycles. *Paleoceanography* **18**, 1036 (2003).
- Bauch, H. A. Interglacial climates and the Atlantic meridional overturning circulation: is there an Arctic controversy? *Quat. Sci. Rev.* **63**, 1–22 (2013).
- Vaks, A. *et al.* Speleothems reveal 500,000-year history of Siberian permafrost. *Science* **340**, 183–186 (2013).
- Froese, D. G., Westgate, J. A., Reyes, A. V., Enkin, R. J. & Preece, S. J. Ancient permafrost and a future, warmer Arctic. *Science* **321**, 1648 (2008).
- Cronin, T. M. *et al.* A 600-ka Arctic sea-ice record from Mendeleev Ridge based on ostracodes. *Quat. Sci. Rev.* **79**, 157–167 (2013).

**Supplementary Information** is available in the online version of the paper.

**Acknowledgements** We thank A. de Vernal for access to pollen records and archived sediment; C. Hillaire-Marcel for discussions of MD99-2227 stratigraphy and geochemistry; J. Briner, B. Hudson, S. Kelley and N. Larsen for providing samples; and E. Colville, P. Holm and S. Strano for assistance in the field. This research was supported by US NSF awards ANS-0902571 (A.E.C., B.L.B.) and -0902751 (J.S.S.), and a Canadian NSERC fellowship (A.V.R.).

**Author Contributions** A.E.C., B.L.B. and J.S.S. had the idea for the study; A.V.R., A.E.C. and R.G.H. designed and conducted field research in Greenland; B.W. conducted grain-size analysis; A.V.R. and B.L.B. conducted isotopic analyses; K.W. sampled and identified foraminifera; A.V.R. and D.J.U. implemented the isotope mixing model; A.E.C., R.G.H., J.S.S. and K.W. developed the age model for MD99-2227; A.V.R., A.E.C. and B.L.B. synthesized the results; and A.V.R. and A.E.C. wrote the manuscript, with input from all authors.

**Author Information** Greenland stream sediment and MD99-2227 data have been deposited with the NOAA National Climatic Data Center ([http://hurrricane.ncdc.noaa.gov/pls/paleox/?p=519:1:0:::P1\\_STUDY\\_ID:16436](http://hurrricane.ncdc.noaa.gov/pls/paleox/?p=519:1:0:::P1_STUDY_ID:16436)). Reprints and permissions information is available at [www.nature.com/reprints](http://www.nature.com/reprints). The authors declare no competing financial interests. Readers are welcome to comment on the online version of the paper. Correspondence and requests for materials should be addressed to A.V.R. (areyes@ualberta.ca) or A.E.C. (acarlson@coas.oregonstate.edu).

## METHODS

**Core MD99-2227: sampling and age model.** Piston core MD99-2227 (58.21° N, 48.37° W, 3,460 m water depth) was collected in 1999 during the IMAGES V cruise aboard RV *Marion Dufresne II*<sup>31</sup>. We collected ~3 cm<sup>3</sup> subsamples of sediment from MD99-2227, typically at 5 cm intervals, between 3,870 and 4,280 cm core depth. These subsamples were separated into sand (>63 µm), silt (3–63 µm) and clay (<3 µm) fractions by wet-sieving (sand) and settling (silt, clay) using Calgon and deionized water. Following size separation, biogenic CaCO<sub>3</sub> and authigenic Fe–Mn coatings were removed from MD99-2227 silts by leaching for ~24 h in 0.1 M HCl with periodic agitation, followed by three H<sub>2</sub>O rinses. Leaching and rinsing was repeated and followed by drying in a ~50 °C oven for ~48 h. The resulting CaCO<sub>3</sub>-free silt was used for all subsequent geochemical analyses. Some palaeoceanographic studies of marine sediment detrital fractions elsewhere in the North Atlantic have been affected by Fe–Mn ‘micronodules’, which tend to have high Pb concentration and anomalously radiogenic Pb isotope composition<sup>32</sup>. It is highly unlikely that our Eirik Drift record is affected by Fe–Mn micronodules because we used HCl to leach the samples, which will dissolve Fe–Mn oxides<sup>33</sup>. Moreover, our Pb isotope data do not record any isotopic excursions towards anomalously radiogenic values (Fig. 2).

The MD99-2227 age model is based primarily on <sup>14</sup>C dates for the 0–30 kyr ago interval<sup>18</sup>, and correlation of relative geomagnetic palaeointensity (RPI) to a global RPI stack<sup>34</sup> and additional δ<sup>18</sup>O tie points for the ~100–150 kyr ago interval<sup>35</sup>. Sedimentation rates defined by the age model are unreliable for the upper ~15 m of MD99-2227 owing to core stretching<sup>19,31</sup> (Extended Data Fig. 5). MIS 11 is a well-defined sedimentary sequence in MD99-2227, based on correlation of *N. pachyderma* (sinistral) δ<sup>18</sup>O and RPI to the LR04 benthic foraminifera oxygen isotope stack<sup>36</sup> and RPI from ODP sites 983 and 1089, respectively<sup>19</sup>. We supplement the original MD99-2227 planktonic δ<sup>18</sup>O record of ref. 19 with 59 recent analyses<sup>35</sup> on *N. pachyderma* (s), and 72 new analyses that were sampled and measured at the Stable Isotope Laboratory at Oregon State University following ref. 35. We further refine the >150-kyr-old portion of the MD99-2227 age model by matching RPI to the PISO-1500 RPI stack<sup>34</sup> using 31 tie points (Extended Data Fig. 4a, b). For the purpose of comparing our MD99-2227 records to pollen concentration at ODP Site 646<sup>4,37</sup>, we placed the ODP Site 646 data on the MD99-2227 age model by matching their bulk magnetic susceptibility records (Extended Data Fig. 4c). Importantly, our conclusions do not hinge on subtle differences of timing arising from age model modifications. Rather, our purpose is to address changes in sediment source during MIS 11 in MD99-2227 and then compare our results with complementary proxy records within the broad MIS 11 interglaciation at ODP Site 646. It is not appropriate to directly compare millennial-scale leads and lags between MD99-2227 and other proxy records owing to age model uncertainties.

**Greenland stream sediments.** Fine-grained glaciofluvial sediments from south Greenland meltwater streams were collected during the summers of 2008, 2009, 2010 and 2011, to substantially add to a stream sediment isotope geochemistry data set reported earlier<sup>16</sup>. We selected 20 samples of glaciofluvial silt, with a focus on samples collected from large, turbid meltwater systems draining major outlet glaciers of the GIS (Extended Data Fig. 3), including one collected for us by B. Hudson. We also analysed four samples of south Greenland glaciolacustrine sediment recently discharged into ice-marginal lakes (Extended Data Fig. 3e; samples collected by N. Larsen, S. Kelley, and J. Briner), five samples of poorly sorted debris entrained in icebergs near calving glacier margins (Extended Data Fig. 3f), and one sample of moraine diamicton. The sediments we sampled represent broad spatial averages of bedrock composition that best reflect the fine sediment produced by subglacial erosion and delivered to the marine sediment core. All samples were size-separated using the same procedure described above for MD99-2227 sediments, but were not acid-leached.

**Isotope geochemistry.** All chemical separation and isotopic analyses were conducted at the University of Wisconsin-Madison Radiogenic Isotope Laboratory. Acids used for sample preparation were purified by sub-boiling distillation, and diluted to ±0.05 M using ultrapure water. Approximately 100 mg of dry sediment from the silt (3–63 µm) size fraction was weighed into Savillex PFA vials and spiked with a mixed <sup>87</sup>Rb–<sup>84</sup>Sr tracer and a rare-earth-element tracer containing <sup>150</sup>Nd and <sup>147</sup>Sm. Spiked samples were digested on hotplates overnight in 3 ml 29 M hydrofluoric acid and 300 µl 14 M HNO<sub>3</sub>, and then evaporated. Next we added 4 ml 29 M hydrofluoric acid and 400 µl 14 M HNO<sub>3</sub>, transferred the slurry to PTFE sleeves in Parr bombs and heated the sealed bombs for 48 h at 180–200 °C. Samples were transferred back to PFA beakers and evaporated, and this was followed by addition of 4 ml 8 M HCl and 24 h of digestion in sealed Parr bombs at 180–200 °C. The samples were inspected for complete mineral dissolution using a binocular microscope before evaporation.

Following sample digestion, we used ion-exchange column chromatography to sequentially separate Pb, Rb–Sr and rare-earth elements. Pb was separated using HBr, HCl and AG1-X8 100–200 mesh anion-exchange resin. Rb–Sr were separated

from the residual eluent using 2.5 M HCl and AG50W-X8 cation-exchange resin, and rare-earth elements were eluted with 6 M HCl. Finally, rare-earth elements were separated using 0.15 M, 0.21 M and 0.5 M 2-methylactic acid and AG50W-X4 cation-exchange resin in NH<sub>3</sub><sup>+</sup> form.

Pb, Rb–Sr and Nd isotope ratios were measured on a VG Sector 54 thermal ionization mass spectrometer; Rb, Sr, Sm and Nd concentrations were determined by isotope dilution. Pb was loaded onto single Re filaments with 1 M H<sub>3</sub>PO<sub>4</sub> and Si gel, and isotope ratios were determined using a static multi-collector analysis. Reported isotope ratios are the mean of 50 ratios measured at a typical <sup>208</sup>Pb ion signal of 2 × 10<sup>-11</sup> amps. Instrument mass bias was corrected by empirically determining a linear mass fractionation correction using the measured <sup>207</sup>Pb/<sup>206</sup>Pb and <sup>208</sup>Pb/<sup>206</sup>Pb ratios of NIST SRM 981 and SRM 982, respectively, run under similar conditions as the samples. Mass fractionation corrections were determined for each analytical session by averaging mass fractionation corrections for three analyses each on SRM 981 and SRM 982. This correction was typically 0.1% per a.m.u. The uncertainty in the mass fractionation correction results in an uncertainty of 0.03% per a.m.u. for Pb isotope ratios. The mean procedural blank for common Pb was ~600 pg (minimum and maximum of 183 and 1,484 pg, respectively), or conservatively <1‰ of the loaded Pb sample.

Sr was loaded on Ta filaments with H<sub>3</sub>PO<sub>4</sub> and analysed using a three-jump dynamic multi-collector analysis routine, with exponential normalization to <sup>86</sup>Sr/<sup>88</sup>Sr = 0.1194. Reported isotope ratios are the mean of 120 ratios with a typical <sup>88</sup>Sr ion signal of 3 × 10<sup>-11</sup> amps. Analysis of NIST SRM 987 yielded mean <sup>87</sup>Sr/<sup>86</sup>Sr of 0.710263 ± 0.000013 (2σ, n = 46). The mean procedural blank for Sr was ~400 pg (minimum and maximum of 114 and 646 pg, respectively) or conservatively <50 p.p.m. of the loaded sample.

Nd was loaded on Re filaments with Si gel and H<sub>3</sub>PO<sub>4</sub>. Isotope ratios were determined as NdO<sup>+</sup> using a dynamic multi-collector analysis routine, with exponential correction for mass fractionation using <sup>146</sup>Nd/<sup>144</sup>Nd = 0.7219. Reported isotope ratios are the mean of 150 ratios with a typical <sup>160</sup>NdO<sup>+</sup> ion signal of 1 × 10<sup>-11</sup> amps. Analyses of internal Nd standards Ames I (n = 17), Ames II (n = 19) and La Jolla (n = 15) yielded mean <sup>143</sup>Nd/<sup>144</sup>Nd (±2σ) of 0.512137 ± 0.000022, 0.511967 ± 0.000015 and 0.511849 ± 0.000020, respectively. The mean procedural blank for Nd was ~200 pg (minimum and maximum of 48 and 730 pg, respectively) or conservatively <0.5‰ of the loaded sample. Nd isotope variations are presented in epsilon notation, which is defined as deviations from the present day <sup>143</sup>Nd/<sup>144</sup>Nd of CHUR (chondritic uniform reservoir) in parts per ten thousand: ε<sub>Nd</sub> = 10,000 × [(<sup>143</sup>Nd/<sup>144</sup>Nd)<sub>sample</sub> / (<sup>143</sup>Nd/<sup>144</sup>Nd)<sub>CHUR</sub> - 1], where CHUR <sup>143</sup>Nd/<sup>144</sup>Nd = 0.512638 (ref. 38).

We carried out identical digestion, element separation and mass spectrometry on a powdered split of USGS reference sample BCR-1, yielding the following values (errors are based on internal counting statistics and are reported as ±2 s.e.): <sup>143</sup>Nd/<sup>144</sup>Nd = 0.512627 ± 0.000008, Nd = 28.4 p.p.m.; <sup>87</sup>Sr/<sup>86</sup>Sr = 0.705033 ± 0.000010, Sr = 327 p.p.m.; <sup>206</sup>Pb/<sup>204</sup>Pb = 18.839 ± 0.002; <sup>207</sup>Pb/<sup>204</sup>Pb = 15.656 ± 0.002; and <sup>208</sup>Pb/<sup>204</sup>Pb = 38.794 ± 0.004. Procedural blanks were negligible compared with sample size, and so no blank corrections were applied. Analytical results for MD99-2227 and stream sediment silts are presented in Supplementary Tables 1 and 2, respectively.

**Geological context and isotope geochemistry of south Greenland terranes.** The bedrock geology of south Greenland is dominated by Precambrian rocks of the KMB, the AB and the NMB. Respectively, these belts are composed of juvenile Proterozoic crust, Archaean basement rocks that were largely unaffected by subsequent tectonism, and Archaean and Proterozoic rocks that were deformed and metamorphosed during Proterozoic tectonism<sup>39–42</sup>. The boundaries of these terranes extend roughly west to east and outcrop from under the ice sheet along the south, east and west coasts<sup>40–42</sup> (Fig. 1). Thus, bedrock from a given terrane in southwest Greenland is similar geochemically to rock from the same terrane in southeast Greenland, on the basis of their broadly similar ages and tectonometamorphic histories. The Palaeogene volcanics are associated with sea-floor spreading. They are present in east-central Greenland and extend across the Denmark Strait to Iceland, and are an important source of silt to the Eirik Drift<sup>15,16,43</sup>.

Rocks of the Proterozoic KMB represent new addition of continental material, rather than reworking of already formed crustal material<sup>44–46</sup>. Stream-sediment silts from the KMB are readily differentiated from AB and NMB sediments by their higher <sup>206</sup>Pb/<sup>204</sup>Pb, <sup>207</sup>Pb/<sup>204</sup>Pb and ε<sub>Nd</sub> (Extended Data Fig. 1a, b, f). KMB silts occupy a distinct field in <sup>87</sup>Rb/<sup>86</sup>Sr space, but concentration-weighted mean <sup>87</sup>Sr/<sup>86</sup>Sr cannot be used to differentiate KMB reliably from the other Precambrian terranes (Extended Data Fig. 1e). Our compilation of KMB whole-rock isotope composition does not include data from the Ilimaussaq intrusion near Narsaq, which has anomalously high ε<sub>Nd</sub> relative to other KMB rocks<sup>16,47</sup>. This intrusion covers ~130 km<sup>2</sup>, or <0.5% of the KMB area, and therefore is insignificant at the terrane-scale for tracking south Greenland sediments.

The AB is made up of gneisses and granite that formed ~2.6–3.1 Gyr ago, with older (>3.6 Gyr old) rocks inland of Nuuk<sup>48</sup>. The AB rocks were not affected by

Proterozoic and Phanerozoic orogenesis and tectonic events<sup>39–42,48,49</sup>. Stream sediment silts from AB watersheds reflect this antiquity, with very low  $\epsilon_{\text{Nd}}$  (Extended Data Fig. 1f; see also ref. 50) and high  $^{87}\text{Sr}/^{86}\text{Sr}$  (Extended Data Fig. 1d). To the north, the NMB is a complex belt of folded and metamorphosed Archaean and Palaeoproterozoic gneisses and granite with local metasedimentary and metavolcanic rocks<sup>49,51</sup>. Although AB and NMB silts occupy distinct fields on  $^{87}\text{Rb}/^{86}\text{Sr}$  and  $^{147}\text{Sm}/^{144}\text{Nd}$  isochron plots (Extended Data Fig. 1d, e), their separation is more problematic when based solely on  $^{87}\text{Sr}/^{86}\text{Sr}$  and  $\epsilon_{\text{Nd}}$  (Extended Data Fig. 1f). Concentration-weighted mean silt  $^{87}\text{Sr}/^{86}\text{Sr}$  is higher for the AB, and AB silts are also differentiable from the NMB on the basis of their lower  $^{207}\text{Pb}/^{204}\text{Pb}$  and  $^{208}\text{Pb}/^{204}\text{Pb}$  (Extended Data Fig. 1a, b).

The Palaeogene volcanic rocks are associated with hotspot volcanism and sea-floor spreading<sup>52,53</sup>. They are predominantly basaltic and have geochemical affinities that overlap with Icelandic basaltic rocks but extend towards isotope compositions of Precambrian Greenlandic crust because of crustal contamination during differentiation<sup>54,55</sup>. We use a compilation of whole-rock<sup>52–57</sup>, and glaciomarine sediment<sup>58,59</sup> isotope composition data to show that Palaeogene volcanic rocks are easily differentiated from the three south Greenland bedrock terranes on the basis of their very low  $^{87}\text{Sr}/^{86}\text{Sr}$  and high  $\epsilon_{\text{Nd}}$  (Extended Data Fig. 1 and Supplementary Table 3).

We considered the possibility that some subglacially eroded silt may be transported to the Eirik Drift from the Caledonian fold belt in northeast Greenland, via the Denmark Strait and the East Greenland Current. However, a study of Holocene and late-glacial clay and silt sedimentation found that although clay-sized sediment from this potential source region is transported to the Eirik Drift, the isotopic composition of the coarser silt size fraction was less consistent with Caledonian fold belt rocks<sup>60</sup>. The Caledonian rocks are composed largely of a spatially heterogeneous assemblage of reworked Precambrian basement rocks similar to the NMB together with minor components of late-Proterozoic/early-Palaeozoic sedimentary rocks and intrusive igneous bodies<sup>61</sup>. We thus expect the Sr–Nd–Pb signature of silt eroded from this terrane to be similar to the NMB, with the Nd isotope composition in particular being relatively insensitive to fractionation during sedimentary reworking. Therefore, our inference of minimal south Greenland Precambrian silt deposition at the Eirik Drift during MIS 11 is robust even if we assume some minor deposition of far-travelled silt from the Caledonian fold belt of northeast Greenland.

**Subglacial erosion and sediment transport.** During glaciations, when the ice-sheet margins extend past the modern shoreline, continental shelf sediments would be reworked and discharged with subglacial meltwater, and ultimately would contribute to the terrigenous silt fraction of MD99–2227. In this way, MD99–2227 silts during full-glacial conditions probably reflect a combination of processes, including subglacial erosion; reworking of shelf sediments deposited during earlier sea-level highstands; ice-rafting from extensive calving margins and drift ice<sup>62</sup>; and turbidites related to submarine mass movements (Extended Data Fig. 6).

In contrast, when ice margins retreat back above the marine limit, subglacial erosion is confined to underlying bedrock and local glacial deposits (Extended Data Fig. 6). Subglacial erosion is high near the margins of the south GIS<sup>7</sup>, and suspended sediment concentrations in Greenland streams have a strong positive correlation to watershed glacier cover<sup>16,22</sup>. Thus, the eroded silt transported by ice-sheet melt water to the ocean, and ultimately to the Eirik Drift via the Western Boundary Undercurrent<sup>63–65</sup>, would reflect local lithologies near the ice-sheet margin.

To minimize the potential for analysis of non-Greenlandic or reworked marine sediments, we did not include in our analyses any MD99–2227 samples from turbidite or detrital carbonate layers<sup>19</sup>. We excluded samples dominated by lithic fragments in the  $>63\ \mu\text{m}$  fraction to reduce the possibility of analysing potentially far-travelled ice-rafted sediment, while acknowledging that silt-dominated ice-rafted sedimentation may occur from both calved glacier ice and drift ice<sup>62</sup>. The negligible weight per cent of sand throughout most of MIS 11 (Fig. 2b) is consistent with minimal ice-rafted debris during this period at nearby IODP Site U1305<sup>20</sup>. The increase in the weight per cent of silt at 4,010–4,000 cm and the increase in the weight per cent of sand at 4,130–4,120 cm were previously identified as turbidite layers, whereas the increase in the weight per cent of sand at 4,240 cm was identified as a detrital carbonate layer from the Laurentide ice sheet<sup>19</sup>.

Winnowing and resuspension of sea-floor sediments have been inferred for some parts of the Eirik Drift, but studies of contemporary linkages between physical oceanography and sedimentology at the Eirik Drift suggest that MD99–2227 is probably not affected by this process because it was collected from water depths  $>500\ \text{m}$  below the present high-velocity core of the Western Boundary Undercurrent<sup>63–65</sup>. The similarity in patterns of sedimentation and interglacial palaeomagnetic signals<sup>17–19</sup> with those observed, at the same depth, 80 km to the south at IODP Site U1305<sup>20,66,67</sup> strongly argues for sediment continuity controlled by, and reflective of, large-scale processes. Particle-size-specific sediment magnetic records from south Greenland's bedrock terranes also highlight the importance of Greenland-derived silt in sedimentation at the Eirik Drift<sup>68</sup>.

**Isotopic mixing model and terrane endmembers.** We used a four-component mixing model to estimate the relative proportions of terrigenous silt in MD99–2227 that originated from KMB, AB, NMB and Palaeogene volcanic source regions<sup>16,69,70</sup>. Endmember values for the KMB, AB and NMB are based on concentration and isotope composition data of stream sediment silts (Supplementary Table 2), whereas the Palaeogene volcanic endmember values are based on whole-rock data compiled from the literature and analyses of glaciomarine sediments (Supplementary Table 3).

There is broad agreement between our stream sediment silt geochemical data and the whole-rock data compiled in ref. 16, although there are some key differences. Concentration-weighted mean  $^{87}\text{Sr}/^{86}\text{Sr}$  and  $^{87}\text{Rb}/^{86}\text{Sr}$  are much higher in the whole-rock data set (Extended Data Fig. 1c, d) for the three Precambrian terranes, probably reflecting some combination of sampling bias towards high-Rb/Sr rocks or loss of radiogenic Sr during chemical weathering, or both. Concentration-weighted silt  $\epsilon_{\text{Nd}}$  is consistent with whole-rock values, although the range of whole-rock  $\epsilon_{\text{Nd}}$  is quite large, particularly for the AB (Extended Data Fig. 1f). AB whole-rock  $^{206}\text{Pb}/^{204}\text{Pb}$  and  $^{207}\text{Pb}/^{204}\text{Pb}$  also exhibit substantial scatter and lower mean values, relative to stream sediment silt (Extended Data Fig. 1a, b).

We generated 1,000 random combinations of endmember isotope composition and concentration within ten evenly spaced bins between the 0.165 and 0.835 quantiles for each terrane geochemical data set (that is, spanning 67% of the asymmetric probability envelope), for a total of 10,000 random combinations of endmember values. We did not measure the Pb concentration of stream sediment silts by isotope dilution, and Pb concentration was rarely reported in the studies we compiled for the Palaeogene volcanic endmember. Thus, for each of the 10,000 randomly generated endmember combinations, we estimated the Pb concentration for the four terranes using the arithmetic mean of Pb concentration estimated from mean continental crustal Pb/Sr and Pb/Nd ratios<sup>71</sup>.

We implemented the four-component mixing model in R<sup>72</sup> using

$$R_m = [f_{\text{KMB}}(C_e)_{\text{KMB}}(R_e)_{\text{KMB}} + f_{\text{AB}}(C_e)_{\text{AB}}(R_e)_{\text{AB}} + f_{\text{NMB}}(C_e)_{\text{NMB}}(R_e)_{\text{NMB}} + f_{\text{PV}}(C_e)_{\text{PV}}(R_e)_{\text{PV}}] \times [f_{\text{KMB}}(C_e)_{\text{KMB}} + f_{\text{AB}}(C_e)_{\text{AB}} + f_{\text{NMB}}(C_e)_{\text{NMB}} + f_{\text{PV}}(C_e)_{\text{PV}}]^{-1}$$

where  $R_m$  is the modelled isotope ratio ( $\epsilon_{\text{Nd}}$ ,  $^{87}\text{Sr}/^{86}\text{Sr}$ ,  $^{206}\text{Pb}/^{204}\text{Pb}$ ,  $^{207}\text{Pb}/^{204}\text{Pb}$  or  $^{208}\text{Pb}/^{204}\text{Pb}$ ),  $f$  is the terrane fraction of MD99–2227  $\text{CaCO}_3$ -free silt, and  $f_{\text{KMB}} + f_{\text{AB}} + f_{\text{NMB}} + f_{\text{PV}} = 1$ ,  $C_e$  is the endmember concentration for a given element (Sr, Nd or Pb) and  $R_e$  is endmember isotope ratio ( $\epsilon_{\text{Nd}}$ ,  $^{87}\text{Sr}/^{86}\text{Sr}$ ,  $^{206}\text{Pb}/^{204}\text{Pb}$ ,  $^{207}\text{Pb}/^{204}\text{Pb}$  or  $^{208}\text{Pb}/^{204}\text{Pb}$ ).

For each analysed depth interval in MD99–2227, and for each of the 10,000 combinations of endmember concentrations and isotope ratios, the mixing equation was solved by iteratively increasing  $f$  by 0.01 and compiling all values of  $f$  that yielded  $R_m$  within a specified range (1.0 for  $\epsilon_{\text{Nd}}$ , 0.0002 for  $^{87}\text{Sr}/^{86}\text{Sr}$ , 0.2 for  $^{206}\text{Pb}/^{204}\text{Pb}$ , 0.1 for  $^{207}\text{Pb}/^{204}\text{Pb}$  and 0.2 for  $^{208}\text{Pb}/^{204}\text{Pb}$ ) around the measured isotope ratios for that depth interval. Mean and median  $f$  values for each terrane, along with the number of valid solutions, are presented in Supplementary Table 4 for each MIS 11 sample from MD99–2227, along with the  $f$  values associated with the 0.165 and 0.835 quantiles.

Because the range of valid mixing solutions is not always normally distributed, we calculated the flux of  $\text{CaCO}_3$ -free silt from each south Greenland terrane as the product of the median  $f$  value for each terrane, sedimentation rate, dry bulk density<sup>31</sup> and % $\text{CaCO}_3$ -free silt. Uncertainty estimates for sediment flux are provided by the 0.165–0.835 and 0.025–0.975 quantile range of valid mixing model solutions for each terrane, that is, the 67% and 95% confidence intervals (Extended Data Fig. 2). These uncertainty estimates are conservative, because the Monte Carlo procedure for random endmember determination can result in unrealistic combinations of source terrane isotope composition and elemental concentration. It is not possible to quantitatively assess uncertainty in sedimentation rates, which in turn affect inferred sediment flux. Sedimentation rates for MIS 11 at MD99–2227 are of the order of 5–25 cm kyr<sup>-1</sup>.

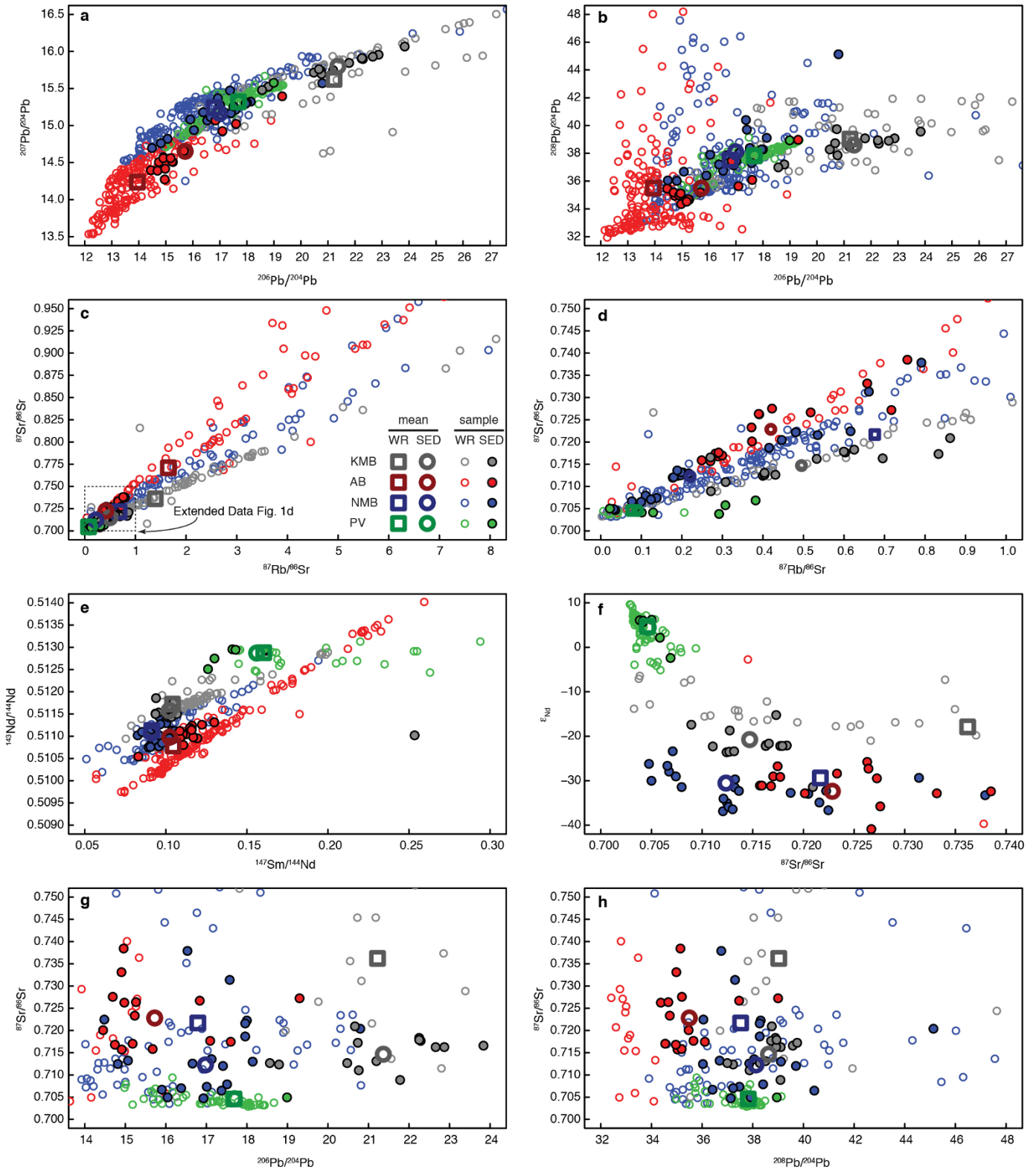
We used the 'prcomp' function in R<sup>72</sup> to conduct a principal-components analysis of the untransformed MIS 11 MD99–2227 isotope composition data, scaled to zero mean and unit variance. The first principal component of the data set represents 73% of the variance and is most strongly correlated to the median ( $r = -0.76$ ) and modal values ( $r = -0.72$ ) for inferred Precambrian Greenlandic silt flux. This finding demonstrates that our interpreted record of  $\text{CaCO}_3$ -free silt flux from Greenland, which is based on independent constraints on source-terrane isotopic composition, represents the most prominent underlying structure in the MD99–2227 geochemical record.

Using this mixing model approach, we also re-analysed the MD99–2227 isotope composition data of ref. 16 for the Holocene and Termination I (Supplementary

Table 5), and the LIG and Termination II (Supplementary Table 6). Our re-analysis results in a greater number of possible mixing equation solutions (Extended Data Fig. 7a). The median  $f$  values are similar to the mean  $f$  values reported in ref. 16, with the most important difference being the slightly greater modelled fraction of CaCO<sub>3</sub>-free silt from the AB in our analysis. We also re-calculate the fractional contribution from each terrane expressed as a percentage of total core sediment (Fig. 3b) because we discovered some isolated and minor errors in the percentage CaCO<sub>3</sub>-free silt and percentage silt data reported in ref. 16. For affected samples, the corrected grain-size data yield increases in estimated silt contribution from the three Precambrian bedrock terranes when expressed as a percentage of the total core sediment (Supplementary Table 7), which only further emphasizes the conclusions of ref. 16. In short, the new mixing model approach and corrected grain-size data do not affect the conclusion that the GIS was present on all three of south Greenland's Precambrian bedrock terranes during the LIG<sup>16</sup>. Indeed, the corrected results underscore the unprecedented nature of the low silt contribution from these terranes during MIS 11 (Fig. 3).

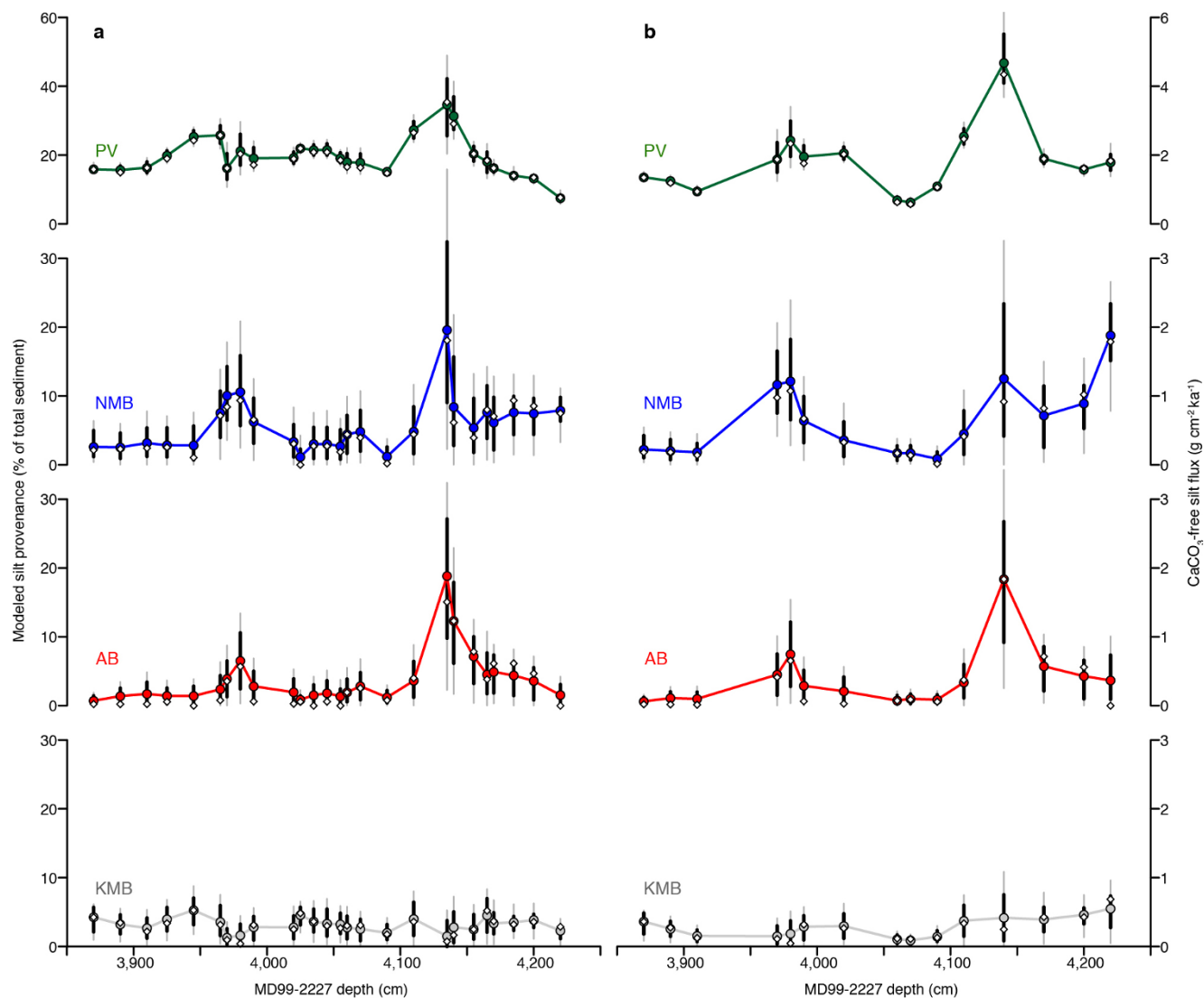
**Comparison to ice-sheet models.** To estimate the sea-level contribution due to MIS 11 GIS retreat, we qualitatively compared our interpretation of a dramatically reduced south GIS with numerical models that simulate GIS response to projected future warming<sup>6,73</sup> or reconstructed MIS 5e climate<sup>9–12,73–78</sup>. We identified model simulations that satisfied our interpretation of largely ice-free AB and NMB; some residual ice on the KMB; ice at Summit Greenland; and ice at coastal north-central east Greenland. The GIS retreat in these simulations<sup>7,9–12</sup> represents a range of global mean sea-level contributions spanning ~4.5 to ~6 m.

31. Hillaire-Marcel, C. *et al.* IMAGES 5 on Board the Marion Dufresne, 2nd Leg 30 June–24 July 1999 (Open File 3782, Geol. Surv. Canada, 1999).
32. Crocket, K. C., Foster, G. L., Vance, D., Richards, D. A. & Tranter, M. A Pb isotope tracer of ocean-ice sheet interaction: the record from the NE Atlantic during the Last Glacial/Interglacial cycle. *Quat. Sci. Rev.* **82**, 133–144 (2013).
33. Michalopoulos, M. & Aller, R. C. Early diagenesis of biogenic silica in the Amazon delta: alteration, authigenic clay formation, and storage. *Geochim. Cosmochim. Acta* **68**, 1061–1085 (2004).
34. Channell, J. E. T., Xuan, C. & Hodell, D. A. Stacking paleointensity and oxygen isotope data for the last 1.5 Myr (PISO-1500). *Earth Planet. Sci. Lett.* **283**, 14–23 (2009).
35. Winsor, K., Carlson, A. E., Klinkhammer, G. P., Stoner, J. S. & Hatfield, R. G. Evolution of the northeast Labrador Sea during the last interglaciation. *Geochem. Geophys. Geosyst.* **13**, Q11006 (2012).
36. Lisiecki, L. E., Raymo, M. E. & A. Pliocene-Pleistocene stack of 57 globally distributed benthic  $\delta^{18}\text{O}$  records. *Paleoceanography* **20**, PA1003 (2005).
37. Aksu, A. E., de Vernal, A. & Mudie, P. J. in *Proc. Ocean Drilling Program, Scientific Results* Vol. 105 (eds. Srivastava, S. P. *et al.*) 617–652 (Ocean Drilling Program, 1989).
38. Jacobsen, S. B. & Wasserburg, G. J. Sm-Nd isotopic evolution of chondrites. *Earth Planet. Sci. Lett.* **50**, 139–155 (1980).
39. Escher, A. & Watt, W. S. in *Geology of Greenland* (eds Escher, A. & Watt, W. S.) 12–15 (Geol. Soc. Greenland, 1976).
40. Birkelund, T., Perch-Nielsen, K., Bridgwater, D. & Higgins, A. K. in *The Ocean Basins and Margins* (eds Nairn, A. E. M. & Stehli, F. G.) 125–159 (Plenum, 1974).
41. Escher, J. C., Ryan, M. J. & Marker, M. in *Precambrian Geology of the Disko Bugt Region, West Greenland* (ed. Kalsbeek, F.) 171–179 (Geol. Greenland Surv. Bull. 181, 1999).
42. Dawes, P. R. The bedrock geology under the Inland Ice: the next major challenge for Greenland mapping. *Geol. Survey Denmark Greenland Bull.* **17**, 57–60 (2009).
43. Fagel, N. *et al.* Nd and Pb isotope signatures of the clay-size fraction of Labrador Sea sediments during the Holocene: implications for the inception of the modern deep circulation pattern. *Paleoceanography* **19**, PA3002 (2004).
44. Patchett, P. J. & Bridgwater, D. Origin of continental crust of 1.9–1.7 Ga age defined by Nd isotopes in the Ketilidian terrain of South Greenland. *Contrib. Mineral. Petrol.* **87**, 311–318 (1984).
45. Van Breemen, O., Aftalion, M. & Allaart, J. H. Isotopic and geochronological studies on granites from the Ketilidian mobile belt of south Greenland. *Geol. Soc. Am. Bull.* **85**, 403–412 (1974).
46. Kalsbeek, F. & Taylor, P. N. Isotopic and chemical variation in granites across a Proterozoic continental margin—the Ketilidian mobile belt of South Greenland. *Earth Planet. Sci. Lett.* **73**, 65–80 (1985).
47. Stevenson, R., Upton, B. G. J. & Steenfelt, A. Crust-mantle interaction in the evolution of the Ilimaussaq Complex, South Greenland: Nd isotopic studies. *Lithos* **40**, 189–202 (1997).
48. Friend, C. R. L. & Nutman, A. P. New pieces to the Archaean terrane jigsaw puzzle in the Nuuk region, southern West Greenland: steps in transforming a simple insight into a complex regional tectonothermal model. *J. Geol. Soc. Lond.* **162**, 147–162 (2005).
49. Henriksen, N., Higgins, A. K., Kalsbeek, F. & Pulvercraft, T. C. R. *Greenland from Archaean to Quaternary. Descriptive Text to the 1995 Geological Map of Greenland, 1:2 500 000* 2nd edn (Geol. Surv. Denmark Greenland Bull. 18, 2009).
50. Goldstein, S. J. & Jacobsen, S. B. Nd and Sr isotopic systematics of river water suspended material - implications for crustal evolution. *Earth Planet. Sci. Lett.* **87**, 249–265 (1988).
51. Whitehouse, M. J., Kalsbeek, F. & Nutman, A. P. Crustal growth and crustal recycling in the Nagsugtoquidian orogen of West Greenland: constraints from radiogenic isotope systematics and U–Pb zircon geochronology. *Precamb. Res.* **91**, 365–381 (1998).
52. Holm, P. M. in *Early Tertiary Volcanism and the Opening of the Northeast Atlantic* (eds Morton, A. C. & Parson, L. M.) 181–196 (Geol. Soc. Spec. Publ. 39, 1988).
53. Bernstein, S. *et al.* Post-breakup basaltic magmatism along the East Greenland Tertiary rifted margin. *Earth Planet. Sci. Lett.* **160**, 845–862 (1998).
54. Hansen, H. & Nielsen, T. F. D. Crustal contamination in Palaeogene East Greenland flood basalts: plumbing system evolution during continental rifting. *Chem. Geol.* **157**, 89–118 (1999).
55. Barker, A. K., Baker, J. A. & Peate, D. W. Interaction of the rifting East Greenland margin with a zoned ancestral Iceland plume. *Geology* **34**, 481–484 (2006).
56. Saunders, A. D., Kempton, P. D., Fittton, J. G. & Larsen, L. M. in *Proc. Ocean Drilling Program, Scientific Results* Vol. 163 (eds Larsen, H.-C., Duncan, R. A., Allan, J. F. & Brooks, K.) 77–93 (Ocean Drilling Program, 1999).
57. Andreassen, R., Peate, D. W. & Brooks, C. K. Magma plumbing systems in large igneous provinces; inferences from cyclical variations in Palaeogene east Greenland basalts. *Contrib. Mineral. Petrol.* **147**, 438–452 (2004).
58. Farmer, G. L., Barber, D. & Andrews, J. Provenance of Late Quaternary ice-proximal sediments in the North Atlantic: Nd, Sr and Pb isotopic evidence. *Earth Planet. Sci. Lett.* **209**, 227–243 (2003).
59. Verplanck, E. P., Farmer, G. L., Andrews, J., Dunhill, G. & Millo, C. Provenance of Quaternary glacial and glaciomarine sediments along the southeast Greenland margin. *Earth Planet. Sci. Lett.* **286**, 52–62 (2009).
60. Innocent, C., Fagel, N. & Hillaire-Marcel, C. Sm-Nd isotope systematics in deep-sea sediments: clay-size versus coarser fractions. *Mar. Geol.* **168**, 79–87 (2000).
61. Higgins, A. K., Gilotto, J. A. & Smith, M. P. (eds) *The Greenland Caledonides: Evolution of the Northeast Margin of Laurentia* (Geol. Soc. Am. Mem. 202, Geological Society of America, 2008).
62. Prins, M. A. *et al.* Ocean circulation and iceberg discharge in the glacial North Atlantic: inferences from unmixing of sediment size distributions. *Geology* **30**, 555–558 (2002).
63. Hunter, S. E. *et al.* Deep western boundary current dynamics and associated sedimentation on the Eirik Drift, Southern Greenland Margin. *Deep-Sea Res.* **54**, 2036–2066 (2007).
64. Innocent, C., Fagel, N., Stevenson, R. K. & Hillaire-Marcel, C. Sm-Nd signature of modern and late Quaternary sediments from the northwest North Atlantic: implications for deep current changes since the Last Glacial Maximum. *Earth Planet. Sci. Lett.* **146**, 607–625 (1997).
65. Stanford, J. D., Rohling, E. J., Bacon, S. & Holliday, N. P. A review of the deep and surface currents around Eirik Drift, south of Greenland: comparison of the past with the present. *Global Planet. Change* **79**, 244–254 (2011).
66. Mazaud, A., Channell, J. E. T. & Stoner, J. S. Relative paleointensity and environmental magnetism since 1.2 Ma at IODP site U1305 (Eirik Drift, NW Atlantic). *Earth Planet. Sci. Lett.* **357–358**, 137–144 (2012).
67. Channell, J. E. T. *et al.* *North Atlantic Climate* (IODP Sci. Prosp. 303/306, Integrated Ocean Drilling Program, 2004).
68. Hatfield, R. G., Stoner, J. S., Carlson, A. E., Reyes, A. V. & Housen, B. A. Source as a controlling factor on the quality and interpretation of sediment magnetic records from the northern North Atlantic. *Earth Planet. Sci. Lett.* **368**, 69–77 (2013).
69. Faure, G. *Principles of Isotope Geology* 141–151 (Wiley, 1986).
70. Albarède, F. *Introduction to Geochemical Modeling* 1–31 (Cambridge Univ. Press, 1995).
71. Rudnick, R. L. & Fountain, D. M. Nature and composition of the continental crust - a lower crustal perspective. *Rev. Geophys.* **33**, 267–309 (1995).
72. R Core Team. *The R Project for Statistical Computing* <http://www.R-project.org> (R Foundation for Statistical Computing, 2013).
73. Fyke, J. G. *et al.* A new coupled ice sheet/climate model: description and sensitivity to model physics under Eemian, Last Glacial Maximum, late Holocene and modern climate conditions. *Geosci. Model Dev.* **4**, 117–136 (2011).
74. Stone, E. J., Lunt, D. J., Annan, J. D. & Hargreaves, J. C. Quantification of the Greenland ice sheet contribution to Last Interglacial sea level rise. *Clim. Past* **9**, 621–639 (2013).
75. Quiquet, A., Ritz, C., Punge, H. J. & Salas y Mélia, D. Greenland ice sheet contribution to sea level rise during the last interglacial period: a modelling study driven and constrained by ice core data. *Clim. Past* **9**, 353–366 (2013).
76. Born, A. & Nansicoglu, K. H. Melting of Northern Greenland during the last interglaciation. *Cryosphere* **6**, 1239–1250 (2012).
77. Helsen, M. M., van de Berg, W. J., van de Wal, R. S. W., van den Broeke, M. R. & Oerlemans, J. Coupled regional climate-ice-sheet simulation shows limited Greenland ice loss during the Eemian. *Clim. Past* **9**, 1773–1788 (2013).
78. Otto-Bliesner, B. *et al.* Simulating Arctic climate warmth and icefield retreat in the last inter-glaciation. *Science* **311**, 1751–1753 (2006).



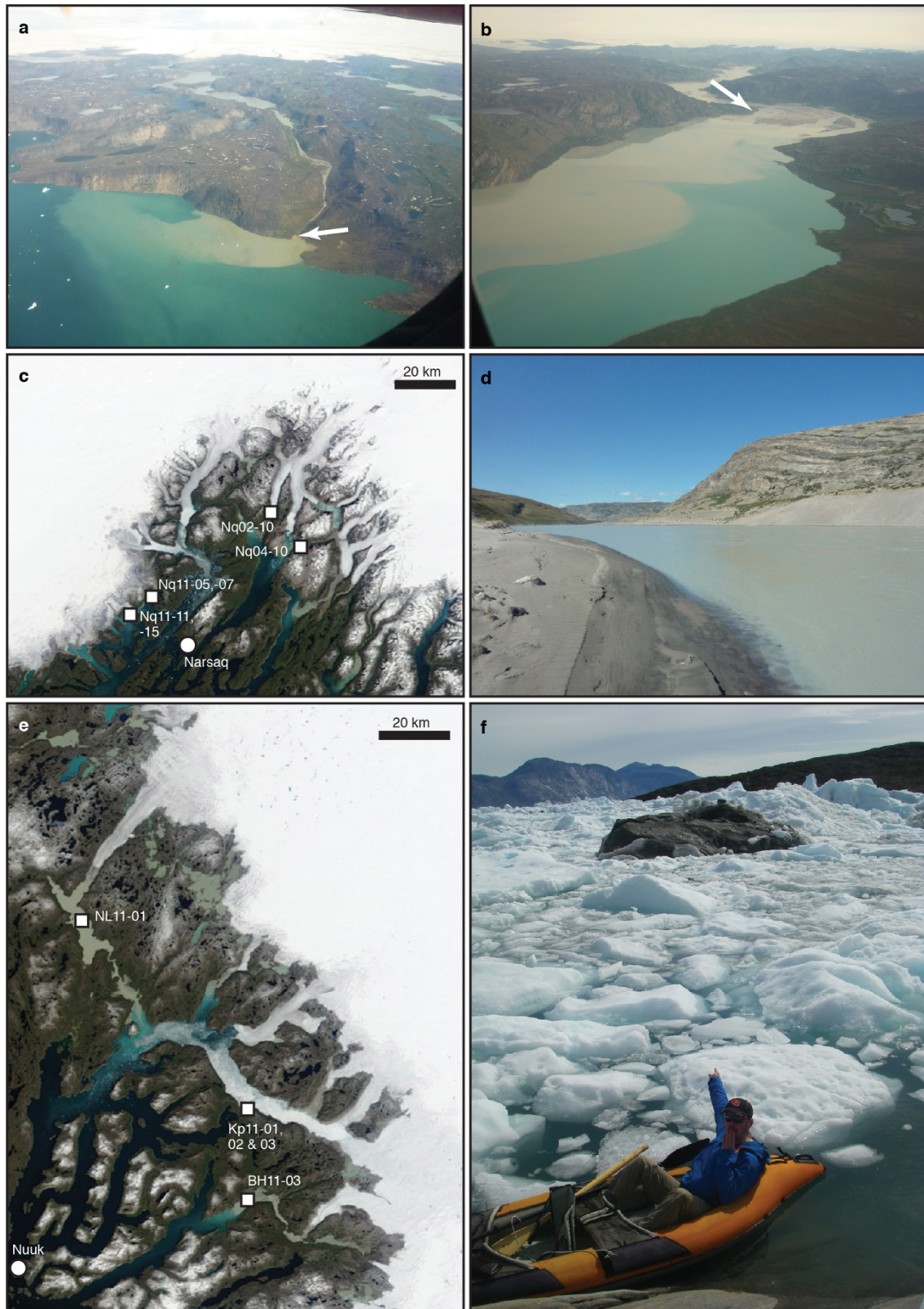
**Extended Data Figure 1 | Whole-rock and stream sediment silt Sr–Nd–Pb isotope composition for south Greenland bedrock terranes. a, b,  $^{207}\text{Pb}/^{204}\text{Pb}$  (a) and  $^{208}\text{Pb}/^{204}\text{Pb}$  (b) versus  $^{206}\text{Pb}/^{204}\text{Pb}$ . c, d,  $^{87}\text{Sr}/^{86}\text{Sr}$  versus  $^{87}\text{Rb}/^{86}\text{Sr}$  for the range of whole-rock (WR) and stream sediment (SED) compositions (c) and restricted to the range of stream sediment compositions (d). e,  $^{143}\text{Nd}/^{144}\text{Nd}$  versus  $^{147}\text{Sm}/^{144}\text{Nd}$ . f,  $\epsilon_{\text{Nd}}$  versus  $^{87}\text{Sr}/^{86}\text{Sr}$ . g, h,  $^{87}\text{Sr}/^{86}\text{Sr}$  versus**

$^{206}\text{Pb}/^{204}\text{Pb}$  (g) and  $^{208}\text{Pb}/^{204}\text{Pb}$  (h). Whole-rock data for KMB, AB and NMB compiled in ref. 16; Palaeogene volcanic whole-rock and glacial shelf sediment data are presented in Supplementary Table 3. Mean values (large symbols) are concentration-weighted means for Rb–Sr and Sm–Nd isotopic compositions, whereas Pb isotope ratios are arithmetic means.



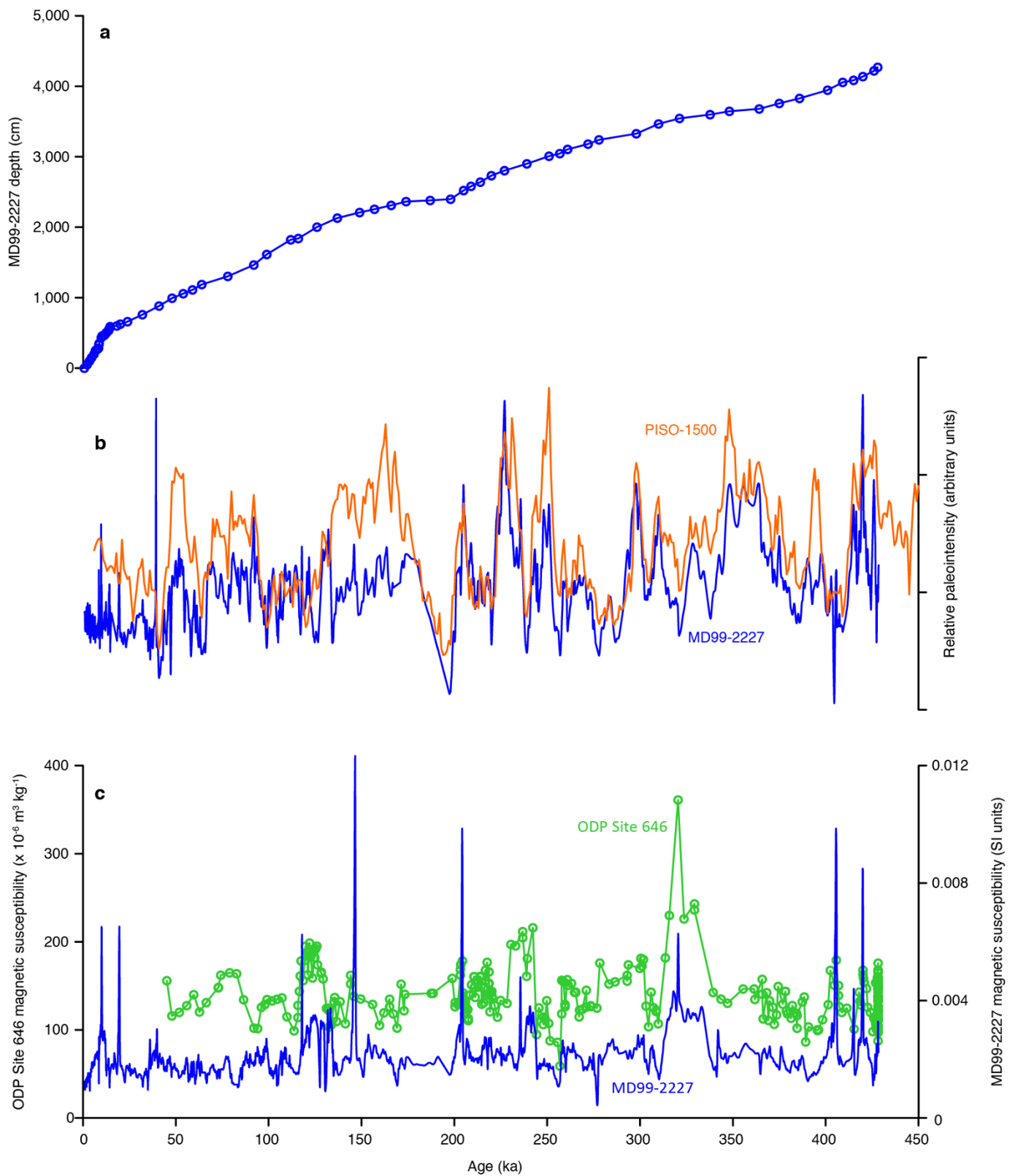
**Extended Data Figure 2 | Summary of mixing model results for each south Greenland terrane.** MD99-2227 inferred silt provenance expressed as median flux of  $\text{CaCO}_3$ -free silt (a) and median percentage of total  $\text{CaCO}_3$ -free silt (b). Values for the Holocene and LIG are recast from  $\text{CaCO}_3$ -free silt Sr–Nd–Pb isotope ratios in ref. 16. Thick black and thin grey vertical lines mark the 16.5–83.5% and 2.5–97.5% quantile ranges, respectively, of valid mixing

solutions from all 10,000 model runs. Uncertainty estimates are conservative, because the Monte Carlo procedure for random endmember determination can result in unrealistic combinations of source-terrane isotope composition and elemental concentration. Note different  $y$ -axis scale for Palaeogene volcanic data.



**Extended Data Figure 3 | Selected sediment sampling sites in west Greenland.** Site coordinates are provided in Supplementary Table 2: **a**, Qa11-04; **b**, Qa11-01; Qa11-03; **c**, stream sediment sampling sites near Narsaq;

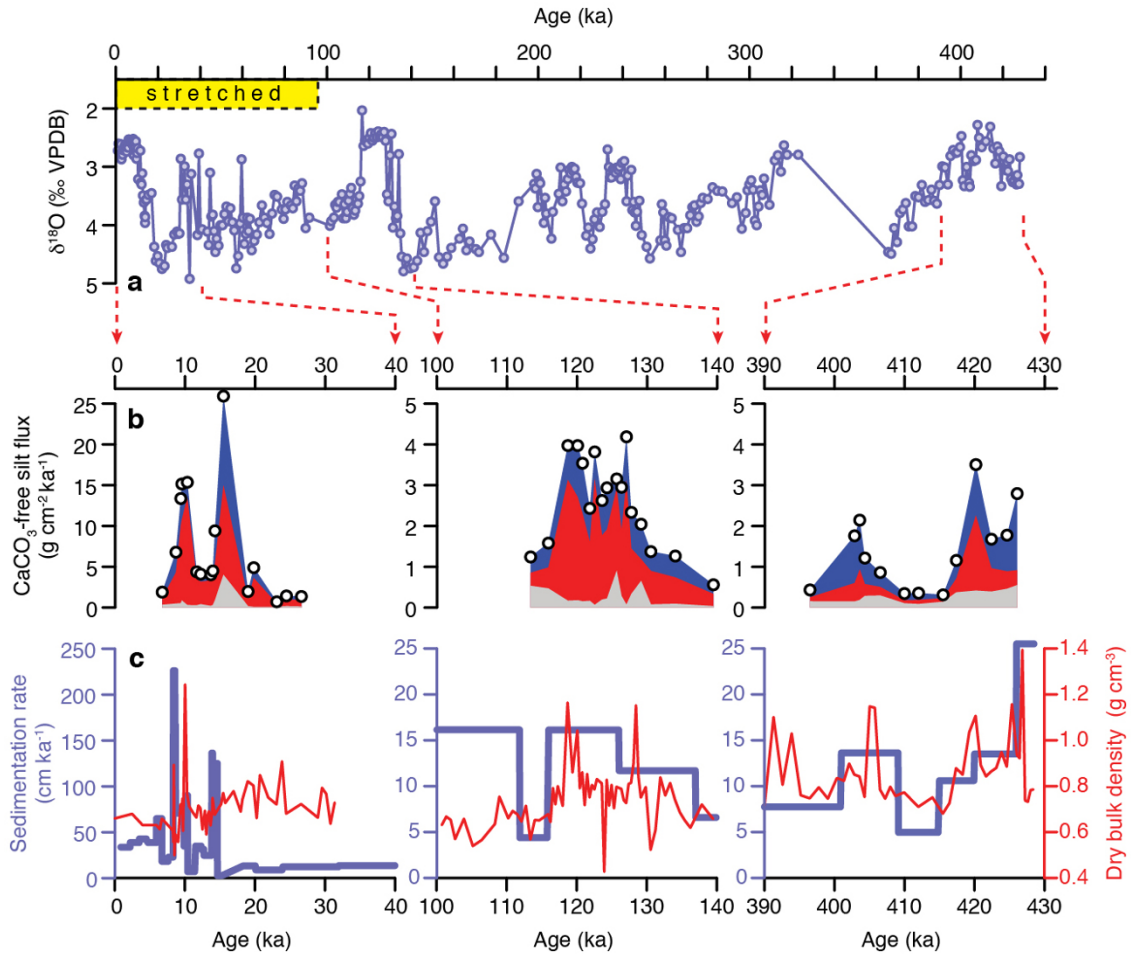
**d**, Kn11-03; **e**, proglacial lake, iceberg debris and proglacial outwash sampling sites near Nuuk; **f**, Kp11-01.



**Extended Data Figure 4 | Age models for MD99-2227 and ODP Site 646.**

**a**, Age–depth model for MD99-2227. Circles mark tie points based on  $^{14}\text{C}$  dates<sup>18</sup>,  $\delta^{18}\text{O}$  (ref. 35) and RPI. **b**, MD99-2227 RPI and the PISO-1500 RPI stack<sup>34</sup>, plotted on their individual age models. Crosses mark RPI tie points.

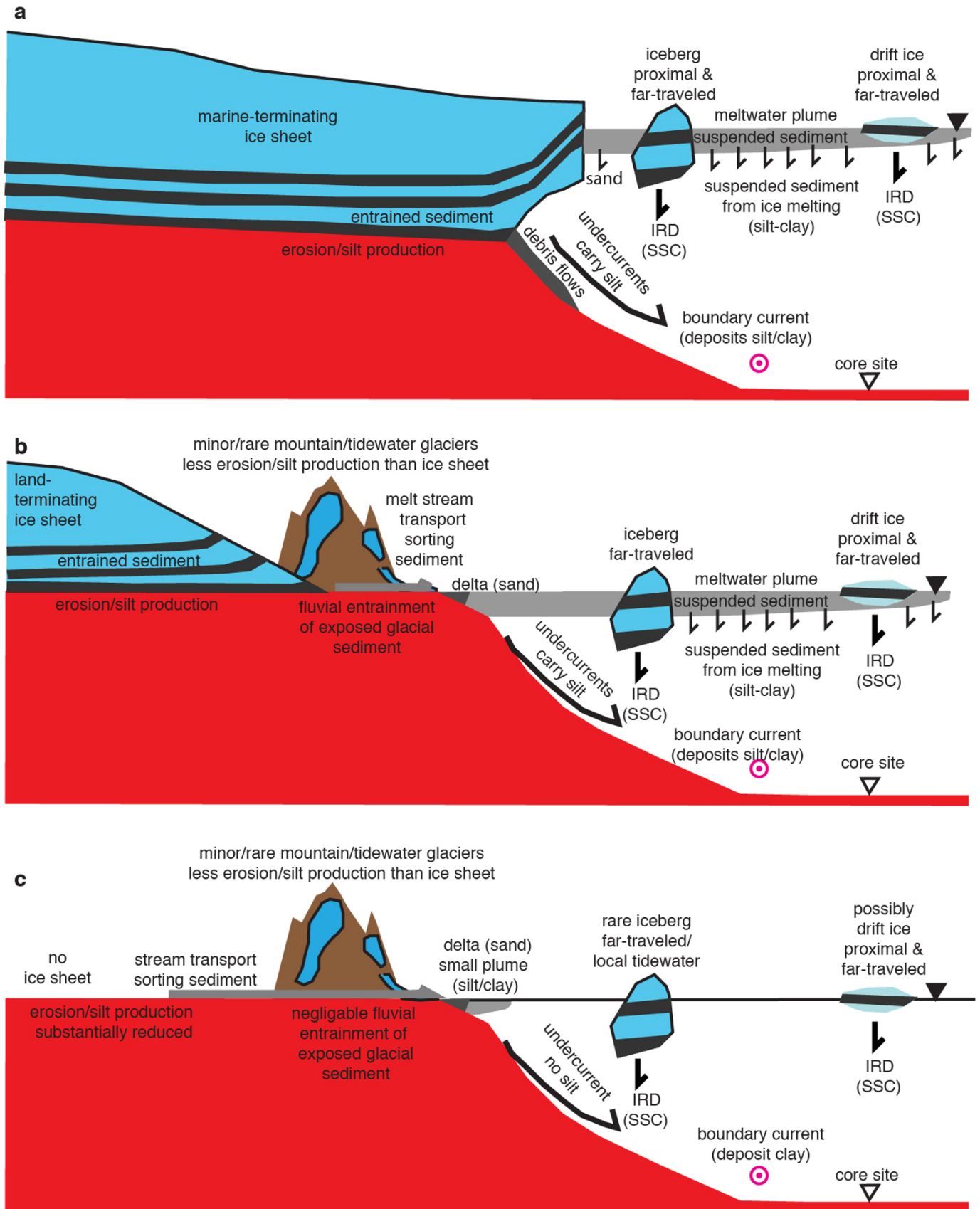
**c**, MD99-2227 and ODP Site 646 magnetic susceptibilities, plotted on the MD99-2227 age model. For comparison purposes, the ODP Site 646 age–depth model was fitted to MD99-2227 using the magnetic susceptibility tie points indicated by crosses.



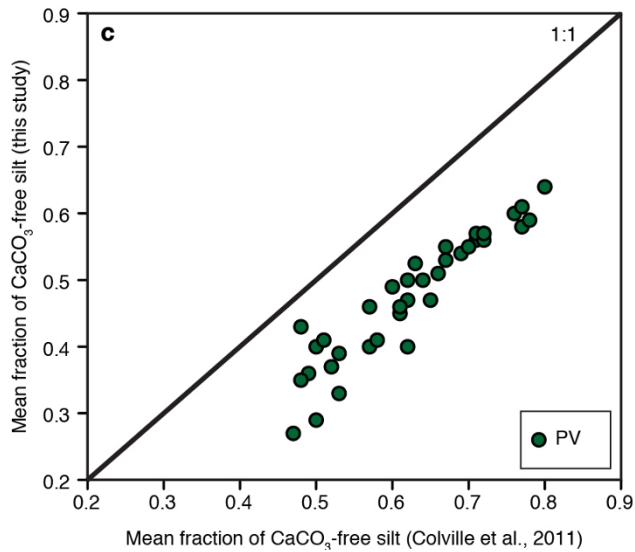
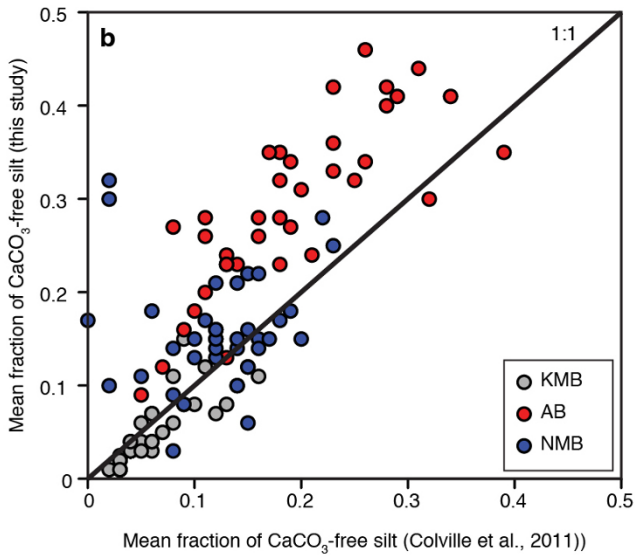
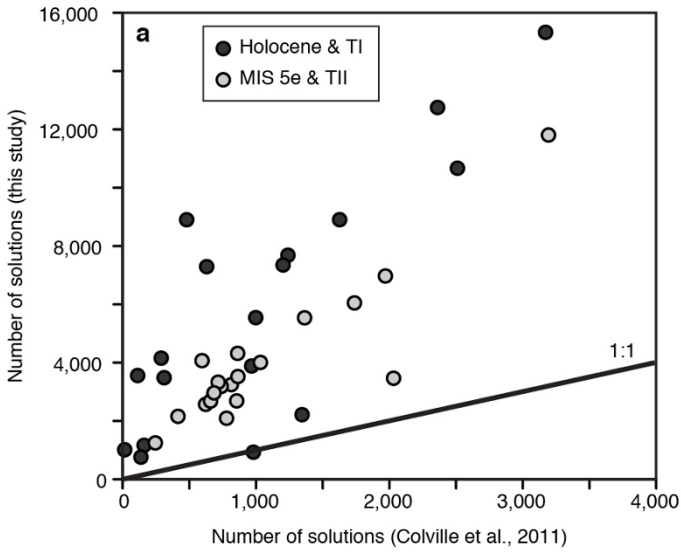
**Extended Data Figure 5 | Comparison of MD99-2227 sedimentation rates and provenance estimates from south Greenland terranes.**

**a,** *Neoglobobadrina pachyderma* (s)  $\delta^{18}\text{O}$  from ODP Site 646 (ref. 4; green) and MD99-2227 (Methods; blue). Yellow bar marks the interval of MD99-2227 that is affected by core stretching. **b,** MD99-2227 inferred silt provenance

estimated using four-component endmember modelling, expressed as flux of  $\text{CaCO}_3$ -free silt. Values for the Holocene and LIG are recast from  $\text{CaCO}_3$ -free silt Sr–Nd–Pb isotope ratios in ref. 16. **c,** MD99-2227 sedimentation rates (left axis, thick blue line) and dry bulk density (right axis, thin red line). Note different y-axis scale for the Holocene/TI panels at far left for **b** and **c**.



**Extended Data Figure 6 | Sediment sources and sedimentation processes.** Conceptual model of terrigenous silt sources and transport processes for a given bedrock terrane during full glaciation (a), glacial termination and deglaciation (b), and near-complete deglaciation (c). SSC, sand/silt/clay.



**Extended Data Figure 7 | Isotope mixing model comparison.** Comparison of mixing model output for MIS 1, Termination I, MIS 5e and Termination II samples presented in ref. 16 with model output using the Monte Carlo approach reported here. **a**, Number of valid mixing equation solutions. **b**, **c**, Mean CaCO<sub>3</sub>-free silt fractions for the KMB, AB and NMB (**b**), and the Palaeogene volcanics (**c**).